

Improved simplified calibration procedure for a high-cycle accumulation model

T. Wichtmannⁱ⁾ A. Niemunisⁱⁱ⁾ Th. Triantafyllidisⁱⁱⁱ⁾

Abstract: The high-cycle accumulation (HCA) model proposed by Niemunis et al. [16] predicts permanent deformations due to a drained cyclic loading with many small cycles (i.e. $N \geq 10^3$ cycles with strain amplitudes $\varepsilon^{\text{ampl}} \leq 10^{-3}$). The strain amplitude is the most important influencing parameter of the rate of strain accumulation $\dot{\varepsilon}^{\text{acc}}$. Based on tests on a medium coarse sand, a square relationship $\dot{\varepsilon}^{\text{acc}} \sim (\varepsilon^{\text{ampl}})^2$ has been used in the HCA model so far. The new test results presented in this paper indicate, however, that the exponent of the amplitude-dependence may vary between 1.3 and 2.4, depending on the tested material. This comes out of 150 drained cyclic triaxial tests with 10^5 load cycles performed on 14 clean quartz sands with specially mixed grain size distribution curves. Consequently, an additional material constant C_{ampl} has been introduced into the HCA model describing the amplitude dependence according to $\dot{\varepsilon}^{\text{acc}} \sim (\varepsilon^{\text{ampl}})^{C_{\text{ampl}}}$. The additional parameter requires a revision of the simplified calibration procedure proposed by Wichtmann et al. [24] which uses correlations between the HCA model parameters and granulometric (d_{50} , C_u) or index properties (e_{min}). Furthermore, the new cyclic test data reveal that the existing correlations are inappropriate for well-graded granular materials ($C_u \geq 5$). Enhanced correlations suitable also for more well-graded sands are proposed in the paper. The possible error of a HCA model prediction with parameters fully or partly determined from the correlations is discussed.

Keywords: drained cyclic triaxial tests, quartz sand, high-cycle accumulation model, simplified calibration, correlations

1 Introduction

High-cycle accumulation (HCA) models predict permanent deformations due to a cyclic loading with many cycles ($N \geq 10^3$) of small to intermediate strain amplitudes ($\varepsilon^{\text{ampl}} \leq 10^{-3}$). Such high-cyclic loading may be caused by traffic (e.g. high-speed railways, magnetic levitation trains), wind and wave action (e.g. onshore and offshore wind power plants), machine foundations (e.g. gas turbines) or repeated filling and emptying processes (e.g. tanks, silos, watergates). Several HCA models have been proposed in the literature. The most recent ones are those of Pasten et al. [17], Karg et al. [10], Abdelkrim et al. [1], Niemunis et al. [16] and Suiker and de Borst [22]. A discussion of older HCA models can be found in [23]. The present paper deals with the model of Niemunis et al. [16]. Recent applications of this model to a gas turbine or to offshore wind power plants are described in [6, 27, 29].

The determination of the parameters used in the HCA model of Niemunis et al. [16], quantifying the dependence of the strain accumulation rate on strain amplitude, void ratio, average stress and cyclic preloading, is quite laborious. The full calibration procedure has been described in detail in [25]. It needs several drained cyclic triaxial tests with different stress amplitudes, initial densities and average stresses. Such calibration for eight different quartz

sands has been documented in [24]. For a simplified calibration, Wichtmann et al. [24] have proposed correlations between the HCA model parameters and granulometric (mean grain size d_{50} , uniformity coefficient $C_u = d_{60}/d_{10}$) or index quantities (minimum void ratio e_{min}). Some or even all parameters of the HCA model can be estimated from these correlations, reducing the number of necessary cyclic laboratory tests. However, some of the correlations proposed in [24] still showed a significant amount of scatter.

In order to confirm the correlations from [24] and to adapt them to a wider range of d_{50} - and C_u -values, 14 additional quartz sands with specially mixed grain size distribution have been tested in approx. 150 drained cyclic triaxial tests. However, the new test results reveal that a revision of the amplitude function used in the HCA model and thus also a revision of the correlation equations used in the simplified calibration procedure is necessary. First, the paper presents the new test results and discusses the observed influence of the grain size distribution curve on the rate of strain accumulation. Afterwards, the revision of the amplitude function and the improved correlations between the HCA model parameters and d_{50} , C_u and e_{min} are presented. An analysis of possible errors made by an estimation of all or parts of the HCA model parameters from these correlations is given.

For a detailed presentation of the equations of the HCA model it is referred to [16] or [24].

The present study is restricted to quartz sands with a subangular grain shape. The dependence of the cumulative deformations under cyclic loading on the mineralogy and the shape of the grains is the subject of our ongoing

ⁱ⁾Researcher, Institute of Soil Mechanics and Rock Mechanics, Karlsruhe Institute of Technology, Germany (corresponding author). Email: torsten.wichtmann@kit.edu

ⁱⁱ⁾Researcher, Institute of Soil Mechanics and Rock Mechanics, Karlsruhe Institute of Technology, Germany

ⁱⁱⁱ⁾Professor and Head of the Institute of Soil Mechanics and Rock Mechanics, Karlsruhe Institute of Technology, Germany

ing research. Sands of different origin, thus having different grain shapes and mineralogy are currently being studied in drained cyclic triaxial tests for that purpose. It is intended to extend the correlations developed for clean quartz sands presented in this paper by these grain characteristics. This work will be presented in a separate publication in future. Some factors being of secondary importance for quartz sands may play an important role for sands with different mineralogy. For example, grain crushing may significantly accelerate the compaction in calcareous sands under cyclic loading. Calcareous sands under drained cyclic loading were tested e.g. in [4, 8, 9, 12]. However, while some authors found a considerable amount of particle breakage (e.g. [4]) some others did not (e.g. [12]).

2 Tested materials and testing procedures

The 14 tested grain size distribution curves with a linear shape in the semi-logarithmic scale are shown in Figure 1. They were mixed from a natural fluvially deposited quartz sand obtained from a sand pit near Dorsten, Germany. Before mixing, the sand has been decomposed into 25 gradations between 0.063 mm and 16 mm grain size. The grain shape is subangular. The influence of mean grain size d_{50} was studied in tests on the sands and gravels L1 to L7 (Figure 1a) which have mean grain sizes in the range $0.1 \text{ mm} \leq d_{50} \leq 3.5 \text{ mm}$ and the same uniformity coefficient $C_u = 1.5$. The C_u -influence was examined in tests on the materials L4 and L10 to L16 (Figure 1b) which have the same mean grain size $d_{50} = 0.6 \text{ mm}$ while C_u varies between 1.5 and 8.

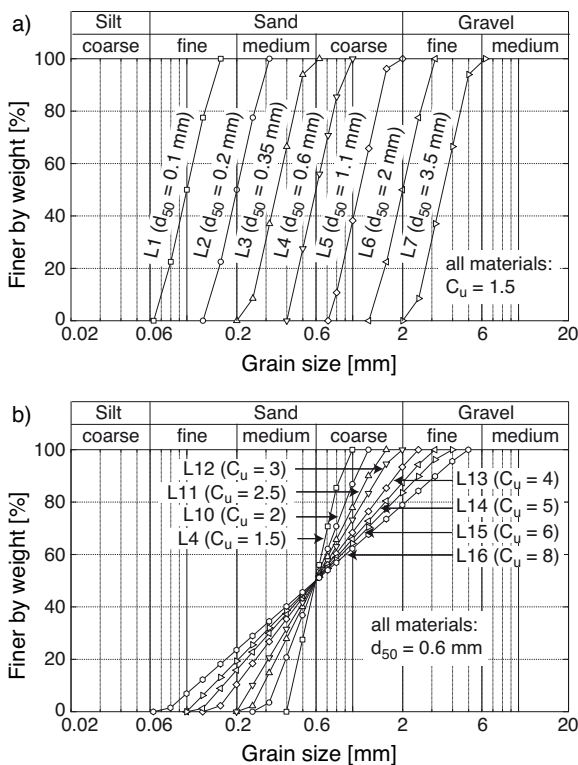


Fig. 1: Tested grain size distribution curves

The cyclic triaxial devices (see the scheme in Figure 2) and the testing procedure applied in the present study were the same as described by Wichtmann et al. [24]. Four similar triaxial devices with a pneumatic loading system were

used for the present study. The samples measuring 10 cm in diameter and 20 cm in height were prepared by air pluviation. Afterwards they were saturated with de-aired water and a back pressure of 200 kPa was applied. The quality of saturation was checked by Skempton's B -value. B -values larger than 0.97 were achieved in all tests. The cell pressure and the axial stress were then increased to the desired average stress of the test. The average stress was kept constant for one hour until the cyclic axial loading was started.

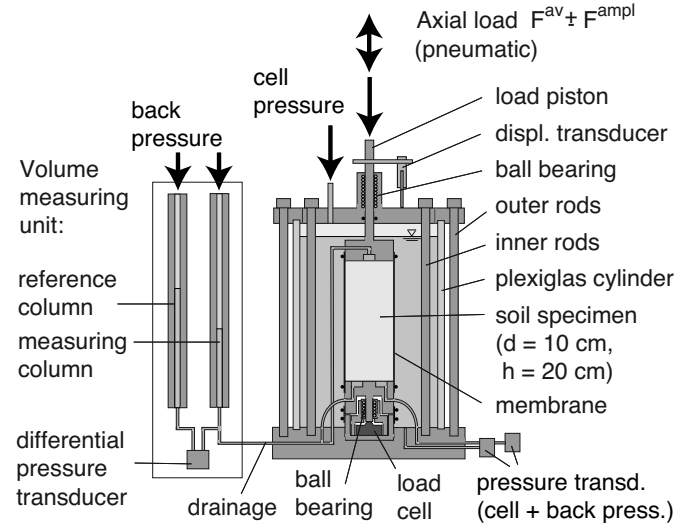


Fig. 2: Scheme of the used triaxial devices

Due to larger deformations the first *irregular* cycle was applied with a low loading frequency of 0.01 Hz while a frequency of 1 Hz was used for the subsequent 100,000 *regular* cycles. The pore pressure measurements showed that free drainage of pore water through the porous stones with 20 mm diameter located in the end plates at both sides of the sample was ensured at this frequency, i.e. no significant oscillation or accumulation of pore water pressure occurred. The only exception was the fine sand L1 where lower frequencies of 0.01 or 0.1 Hz were necessary during the regular cycles in order to guarantee full drainage. In that case only 2,000 or 10,000 regular cycles were tested.

The axial deformation was measured with a displacement transducer attached to the load piston (Figure 2). The system compliance was determined in preliminary tests on a steel dummy and subtracted from the measured values. Volume changes were determined via the squeezed out pore water using a burette system and a differential pressure transducer. The axial load was measured at a load cell located inside the pressure cell below the bottom of the sample. Two pressure transducers were used for monitoring cell pressure and back pressure. The data were recorded during the first 25 cycles and during five cycles at $N = 50, 100, 200, 500, \dots, 5 \cdot 10^4$ and 10^5 . Typical recorded data in terms of the axial strain ε_1 are given in Figure 3. From such data the elastic ($\varepsilon_1^{\text{ampl}}$) and plastic ($\varepsilon_1^{\text{acc}}$) portions of strain have been evaluated as demonstrated in Figure 4. For a more detailed explanation of the analysis of the raw test data it is referred to [25].

For each sand four series of drained cyclic triaxial tests were performed. The effective stress paths are shown schematically in Figure 5. In the first series (Figure 5a) three different deviatoric stress amplitudes q^{ampl} between

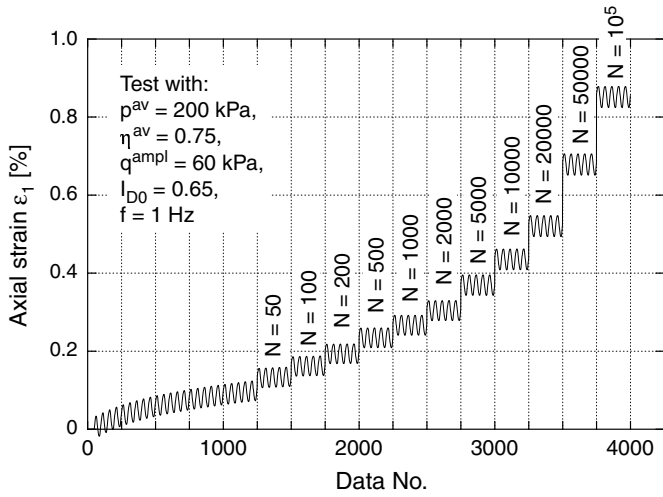


Fig. 3: Increase of the axial strain with the number of cycles in a drained cyclic triaxial test on sand L2

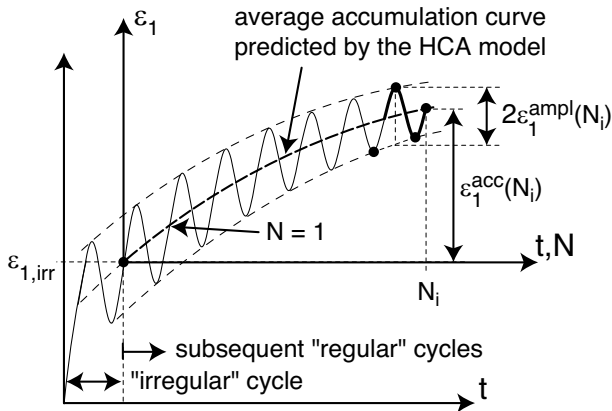


Fig. 4: Distinction between the first irregular and the subsequent regular cycles; Determination of strain amplitude $\varepsilon_1^{\text{ampl}}$ and accumulated strain $\varepsilon_1^{\text{acc}}$ from the recorded data $\varepsilon_1(t)$

20 and 80 kPa were tested, while the average stress σ^{av} was kept constant. The initial densities of the samples were similar. In the second series (Figure 5b), the initial relative density $I_{D0} = (e_{\text{max}} - e)/(e_{\text{max}} - e_{\text{min}})$ was varied between medium dense and dense, keeping the average and cyclic stresses constant. For each material three or four different densities were tested. The third test series (Figure 5c) was performed with different average mean pressures in the range $50 \text{ kPa} \leq p^{\text{av}} \leq 300 \text{ kPa}$. The average stress ratio $\eta^{\text{av}} = q^{\text{av}}/p^{\text{av}}$ and the amplitude-pressure ratio $\zeta = q^{\text{ampl}}/p^{\text{av}}$ were the same in the four tests performed for each sand. Finally, in the fourth test series (Figure 5d) the average stress ratio η^{av} was varied between 0.50 and 1.25. In the four tests performed for each sand, the average mean pressure and the stress amplitude were constant. Each test was performed on a fresh sample (i.e. no multistage testing).

Since the HCA model predicts the accumulation due to the regular cycles only (see Figure 4), the first irregular cycle is not discussed in this paper.

Particle breakage has been examined on the medium coarse sand S3 ($d_{50} = 0.55 \text{ mm}$, $C_u = 1.8$, see Table 2) tested in [24]. A sieve analysis using the standard sieves

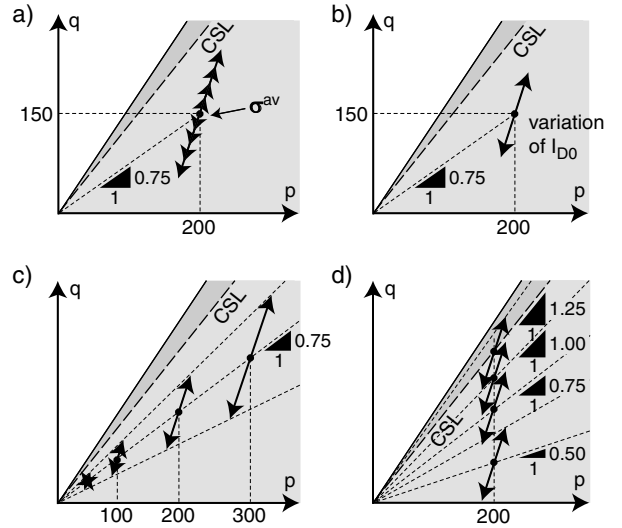


Fig. 5: Effective stress paths in the four series of cyclic triaxial tests performed on each sand: a) different deviatoric stress amplitudes q^{ampl} , b) different initial relative densities I_{D0} , c) different average mean pressures p^{av} at a constant average stress ratio $\eta^{\text{av}} = q^{\text{av}}/p^{\text{av}}$ and d) different average stress ratios η^{av} at a constant value of p^{av}

complemented by several intermediate sieves (similar to the sieving curves presented in Figure 1) has been undertaken before and after the application of 10^5 cycles. No significant change of the grain size distribution curve due to the cycles, that means no particle breakage could be detected. However, it should be kept in mind that the accuracy of such sieve analysis is limited. An automated grain shape analysis (similar to that described in [3]) using the program ImageJ and pictures of the grains taken with a scanner has been performed on another quartz sand (Karlsruhe sand, $d_{50} = 0.56 \text{ mm}$, $C_u = 1.5$). The grain shape parameters (e.g. circularity, compactness, aspect ratio) determined before and after a cyclic test were similar. Therefore, particle breakage has not been further studied in the framework of the current experimental study. However, it should be mentioned that particle breakage due to cyclic loading has been observed also for quartz sands [11].

3 Test results

As observed in the earlier study [24], the direction of strain accumulation $\dot{\varepsilon}_q^{\text{acc}}/\dot{\varepsilon}_v^{\text{acc}}$, i.e. the ratio of deviatoric and volumetric strain accumulation rates ($\varepsilon_v = \varepsilon_1 + 2\varepsilon_3$, $\varepsilon_q = 2/3(\varepsilon_1 - \varepsilon_3)$, the dot $\dot{}$ denotes a derivative with respect to the number of cycles N), was found independent of stress amplitude, initial density and average mean pressure for all tested sands. This is evident from Figure 6a-c where the accumulated deviatoric strain $\varepsilon_q^{\text{acc}}$ is plotted versus the accumulated volumetric strain $\varepsilon_v^{\text{acc}}$. The data are shown exemplary for selected sands. The directions of the $\varepsilon_q^{\text{acc}} - \varepsilon_v^{\text{acc}}$ strain paths from tests with different amplitudes (Figure 6a), initial densities (Figure 6b) and average mean pressures (Figure 6c) coincide. A similar dependence of $\dot{\varepsilon}_q^{\text{acc}}/\dot{\varepsilon}_v^{\text{acc}}$ on average stress ratio $\eta^{\text{av}} = q^{\text{av}}/p^{\text{av}}$ as reported in [2,13,24] was found in the present test series. The increase of the deviatoric portion of the strain accumulation rate with increasing average stress ratio $\eta^{\text{av}} = q^{\text{av}}/p^{\text{av}}$

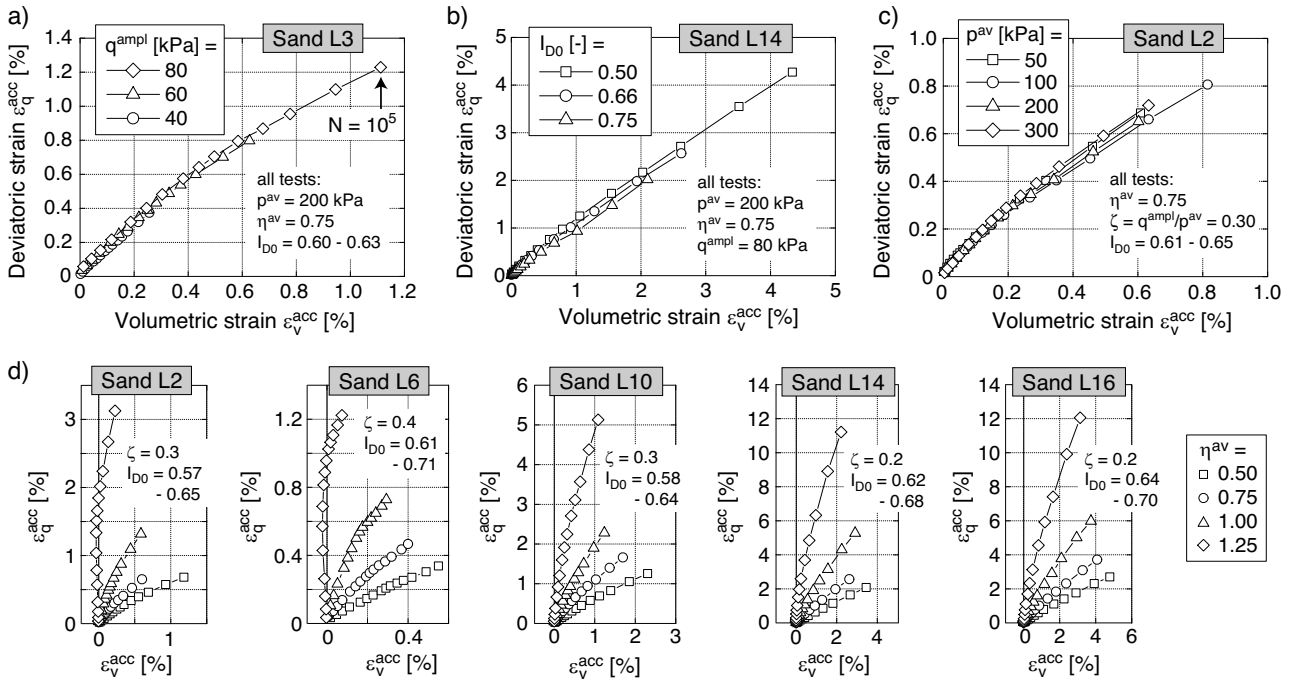


Fig. 6: $\varepsilon_q^{\text{acc}}-\varepsilon_v^{\text{acc}}$ strain paths in tests with different a) stress amplitudes q^{ampl} , b) initial relative densities I_{D0} , c) average mean pressures p^{av} and d) average stress ratios η^{av}

becomes clear from the $\varepsilon_q^{\text{acc}}-\varepsilon_v^{\text{acc}}$ strain paths shown for selected materials and different values of η^{av} in Figure 6d. Based on the data from the present test series the direction of strain accumulation (tensor \mathbf{m} in the HCA model) is discussed in more detail in [26]. Therefore, a deeper inspection of \mathbf{m} is let out in the present paper. In the following, the presentation of the test results concentrates on the intensity of strain accumulation $\dot{\varepsilon}^{\text{acc}} = \partial\varepsilon^{\text{acc}}/\partial N$, with ε being the norm of the strain tensor, i.e. $\varepsilon = \sqrt{\varepsilon_1^2 + 2\varepsilon_3^2}$.

For some of the tested materials, the curves of permanent strain ε^{acc} versus number of cycles N measured in three tests with different stress amplitudes ($20 \text{ kPa} \leq q^{\text{ampl}} \leq 80 \text{ kPa}$) are presented in Figure 7. All other parameters (I_{D0} , $p^{\text{av}} = 200 \text{ kPa}$, $\eta^{\text{av}} = 0.75$) were kept constant in these tests. The increase of the intensity of strain accumulation $\dot{\varepsilon}^{\text{acc}}$ with increasing stress amplitude, which is evident in Figure 7, agrees well with results in the literature [5, 14, 18–21, 28]. In Figure 8 the permanent strain after different numbers of cycles is given as a function of strain amplitude. Since the strain amplitude slightly varied with the number of cycles in the stress-controlled tests, a mean value $\bar{\varepsilon}^{\text{ampl}} = 1/N \int \varepsilon^{\text{ampl}}(N) dN$ has been used on the abscissa. The permanent strain on the ordinate has been slightly corrected by dividing it through the void ratio function \bar{f}_e of the HCA model. In that way the data have been purified from the influence of slightly different initial void ratios e_0 and different compaction rates \dot{e} due to the different stress amplitudes. The void ratio function \bar{f}_e has been evaluated with a mean value of void ratio $\bar{e} = 1/N \int e(N) dN$. The calibration of the HCA model functions for the various sands (amongst others f_e) is discussed in the next section. The data in Figure 8 confirm the disproportionate increase of the intensity of accumulation with increasing strain amplitude reported in [24].

However, the data in Figure 8 do not always obey $\varepsilon^{\text{acc}}/\bar{f}_e \sim (\bar{\varepsilon}^{\text{ampl}})^2$. The exponent 2 of the relationship be-

tween $\dot{\varepsilon}^{\text{acc}}$ and $\varepsilon^{\text{ampl}}$ was one of the major assumptions in the HCA model so far. It was corroborated by some other experimental studies in the literature [14, 18, 19]. The new test results show, however, that this exponent can be significantly lower than 2 for some materials while it is higher for some other sands. These findings necessitate a reformulation of the HCA model function f_{ampl} (see next section).

The influence of the grain size distribution curve on the rate of strain accumulation is inspected in Figure 9. The permanent strain after 10,000 cycles is plotted versus mean grain size d_{50} or versus the uniformity coefficient C_u , respectively. All specimens were medium dense (see the ranges of relative densities provided in Figure 7). In accordance with the results reported by Wichtmann et al. [24] the intensity of accumulation increases with decreasing mean grain size and with increasing uniformity coefficient.

The lower accumulation rates for larger grains may be due to a systematic change of grain shape or surface roughness with varying d_{50} . However, an automated grain shape analysis (as described in Section 2) performed on the sands of the present study after the completion of all tests did not show a systematic dependence of grain shape parameters like circularity, compactness or aspect ratio on grain size. The lower total number of grains in a sample with larger grain size could be another reason for the d_{50} -dependence observed in the triaxial tests. Inhomogeneities in the granular packing, leading to larger accumulation rates, become more likely with increasing number of grains. A respective study with cyclic tests on samples of different size is planned for the future.

A large uniformity coefficient C_u corresponds to a granular packing that consists of particles with a wide range of grain sizes. The recent experimental findings agree well with practical experience from vibratory compaction construction sites that well-graded granular materials can be

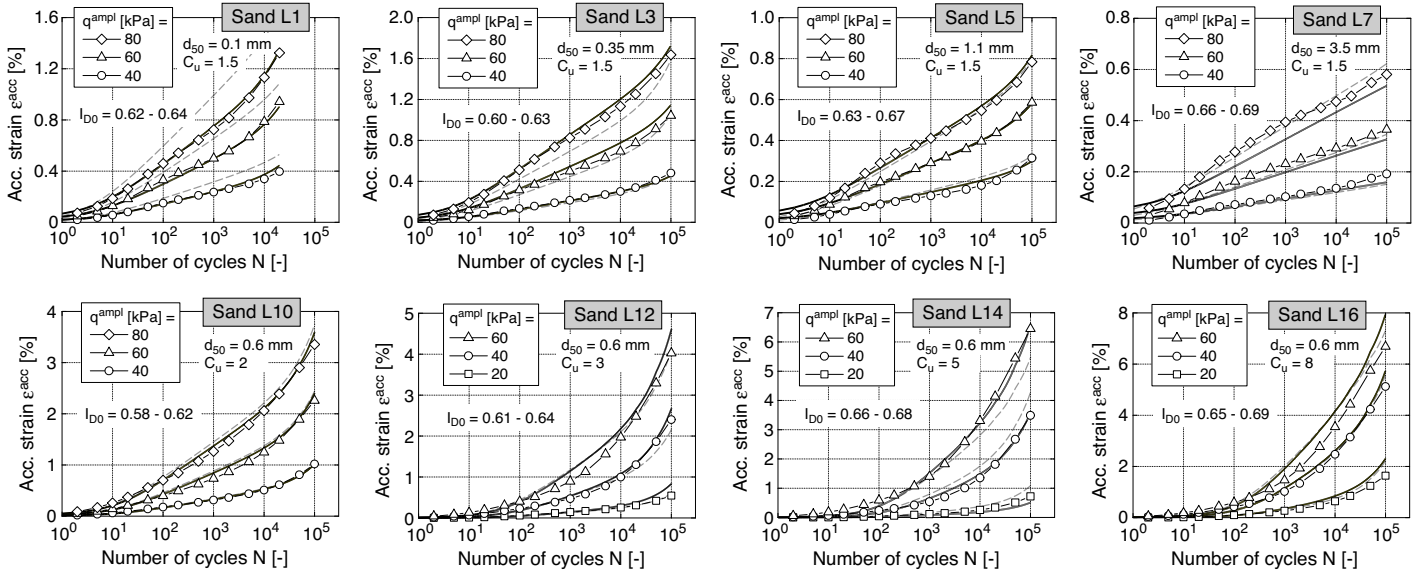


Fig. 7: Accumulation curves $\varepsilon^{acc}(N)$ measured in tests with different stress amplitudes q^{amp} (all tests: $p^{av} = 200$ kPa, $\eta^{av} = 0.75$). Black solid curves = recalculation with HCA model and parameters in columns 14 to 20 of Table 2. Gray dashed curves = recalculation with parameters estimated from correlations (2) to (8).

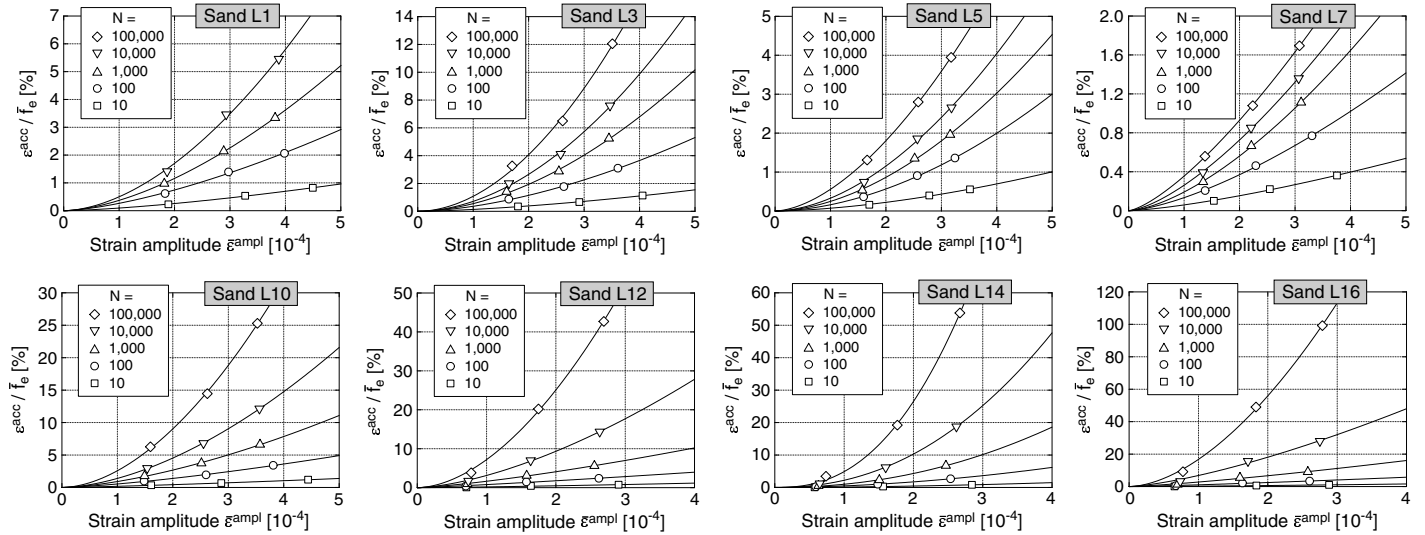


Fig. 8: Accumulated strain $\varepsilon^{acc}/\bar{f}_e$ as a function of a mean value of strain amplitude $\bar{\varepsilon}^{amp} = 1/N \int \varepsilon^{amp}(N)dN$ (solid curves = fitting of HCA model function f_{amp} , see Table 1)

compacted more effectively than rather uniform materials composed of particles with similar size.

Figures 10 and 11 show results from the test series with varying initial density of the specimens. The average stress and the stress amplitude were kept constant within the tests on a certain material. The accumulation curves $\varepsilon^{acc}(N)$ provided in Figure 10 and the plots of the permanent strain ε^{acc} versus a mean value of void ratio \bar{e} in Figure 11 demonstrate the increase of the rate of strain accumulation with decreasing density, i.e. increasing void ratio. This is in good accordance with the test results shown in [5, 7, 14, 20, 21, 24, 28]. In Figure 11 the permanent strain ε^{acc} has been divided by the amplitude function \bar{f}_{amp} in order to purify the data from the influence of slightly different strain amplitudes. The strain amplitude ε^{amp} is somewhat larger for lower initial densities.

The accumulation curves $\varepsilon^{acc}(N)$ measured in the tests with different average mean pressures p^{av} are given in Figure 12. These test series were performed on medium dense

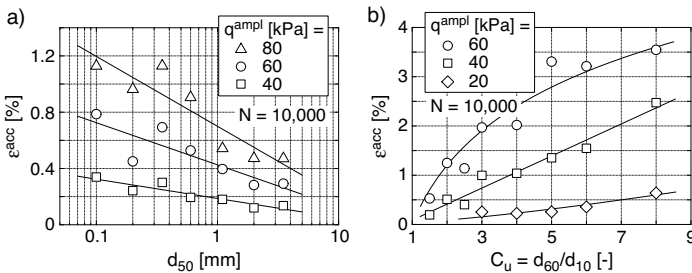


Fig. 9: Accumulated strain ε^{acc} after 10,000 cycles as a function of a) mean grain size d_{50} (data from sands L1 to L7) and b) uniformity coefficient C_u (data from sands L4 and L10 to L16)

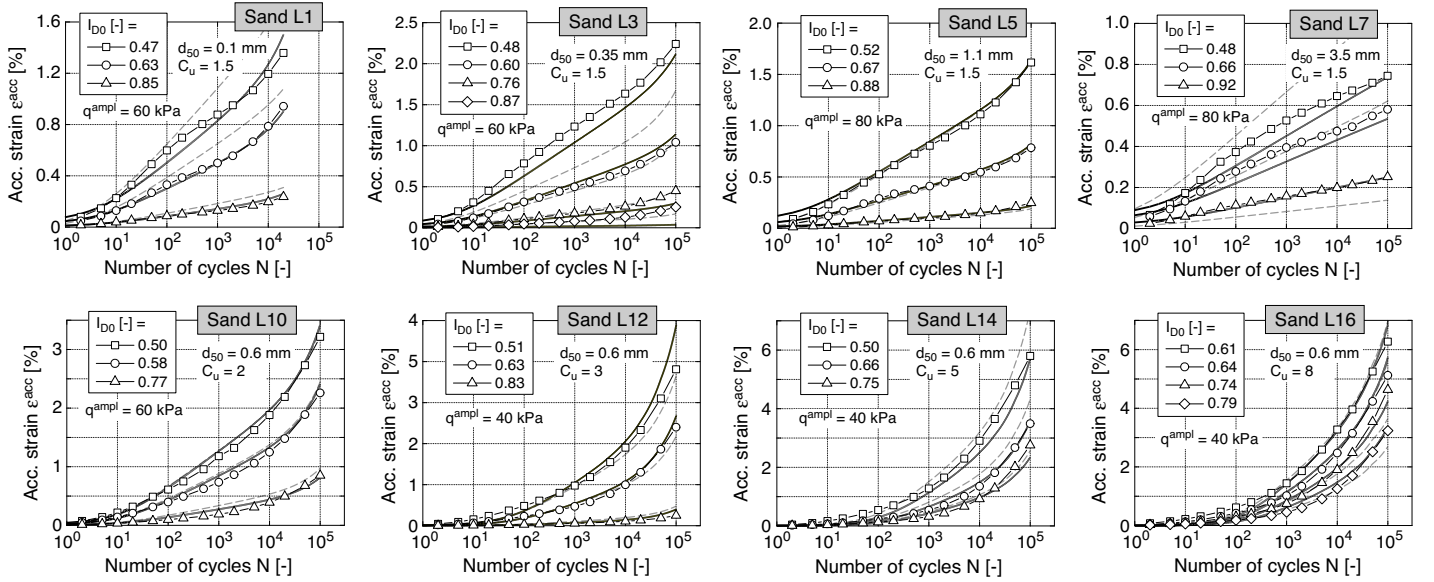


Fig. 10: Accumulation curves $\varepsilon^{\text{acc}}(N)$ measured in tests with different initial relative densities I_{D0} (all tests: $p^{\text{av}} = 200 \text{ kPa}$, $\eta^{\text{av}} = 0.75$). Black solid curves = recalculation with HCA model and parameters in columns 14 to 20 of Table 2. Gray dashed curves = recalculation with parameters estimated from correlations (2) to (8).

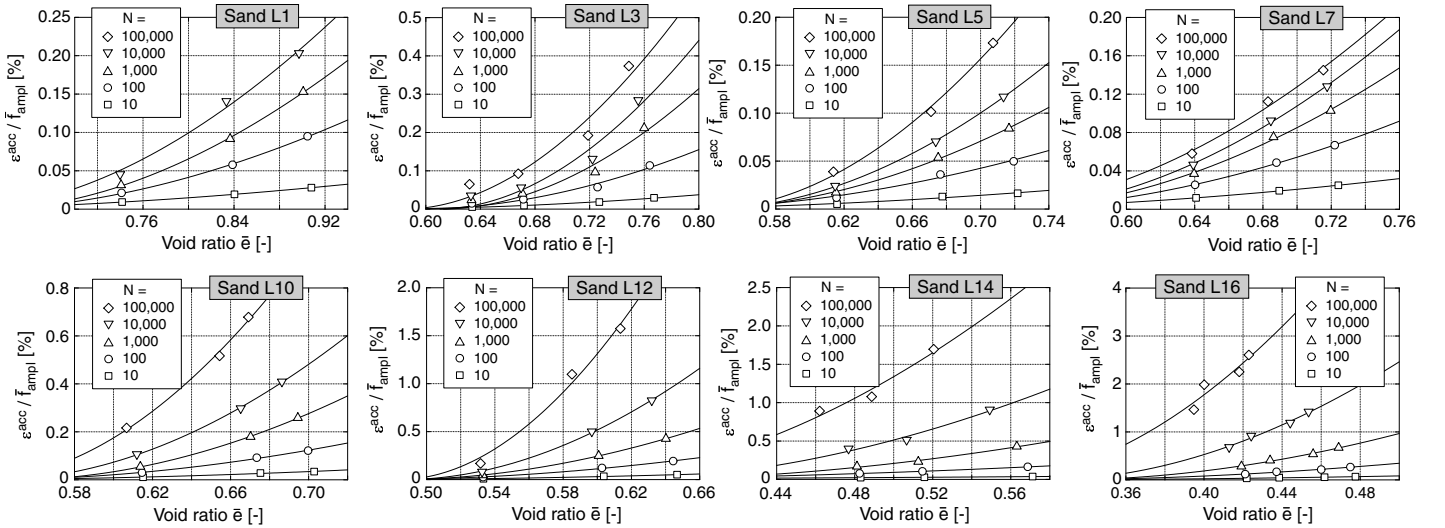


Fig. 11: Accumulated strain $\varepsilon^{\text{acc}}/f^{\text{ampl}}$ as a function of a mean value of void ratio $\bar{e} = 1/N \int e(N)dN$ (solid curves = fitting of HCA model function f_e , see Table 1)

specimens, with a constant average stress ratio $\eta^{\text{av}} = 0.75$ and a constant amplitude-pressure ratio $\zeta = q^{\text{ampl}}/p^{\text{av}}$. The amplitude-pressure ratio ζ was chosen lower for sands showing larger accumulation rates, i.e. it was $\zeta = 0.2$ for the well-graded sands and $\zeta = 0.4$ for the coarse uniform sands. For a certain material, the accumulation curves $\varepsilon^{\text{acc}}(N)$ measured for different average mean pressure nearly coincide (Figure 12). The curves for the lowest tested pressure $p^{\text{av}} = 50 \text{ kPa}$ lie at the upper bound of the $\varepsilon^{\text{acc}}(N)$ data for some materials (e.g. L12) while they are located at the lower bound in some other cases (in particular in case of gravel L7). This is due to the fact that the pressure-dependence of the strain accumulation rate $\dot{\varepsilon}^{\text{acc}}$ depends on the grain size distribution curve (Figure 13).

Keeping η^{av} and ζ constant implies an increase of the strain amplitude with increasing average mean pressure due to the pressure-dependence of the secant stiffness [24]. The

different strain amplitudes have been considered in Figure 13 where the permanent strain has been divided by the amplitude and void ratio functions of the HCA model and plotted versus p^{av} . The decrease of the intensity of accumulation with increasing average mean pressure is obvious in Figure 13. It agrees well with the simple shear test data in [5]. The p^{av} -dependence of $\dot{\varepsilon}^{\text{acc}}$ becomes more pronounced with increasing number of cycles but less pronounced with increasing mean grain size d_{50} of the tested material. For the coarsest tested material L7 the pressure-dependence of the rate of strain accumulation is very small, in particular for higher N -values (Figure 13).

An increase of the rate of strain accumulation with increasing average stress ratio η^{av} was observed for all tested materials. It becomes clear from Figures 14 and 15, which compare the strain accumulation curves $\varepsilon^{\text{acc}}(N)$ for different η^{av} -values or show the permanent strain after different

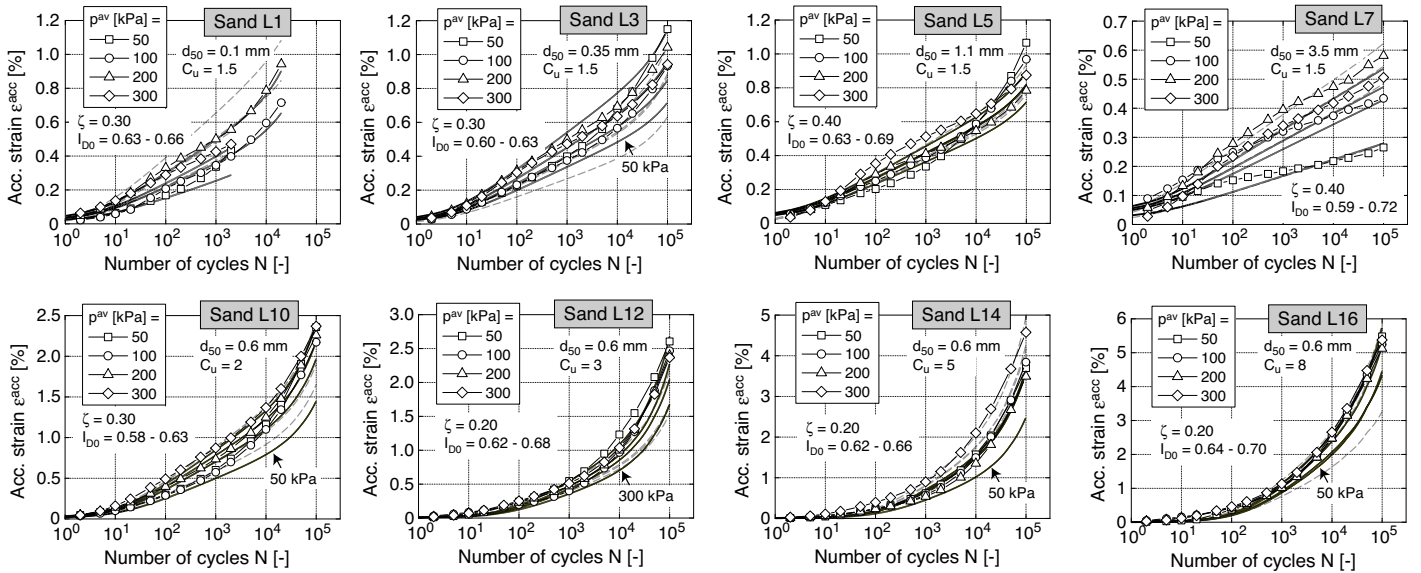


Fig. 12: Accumulation curves $\varepsilon^{\text{acc}}(N)$ measured in tests with different average mean pressures p^{av} (all tests: $\eta^{\text{av}} = 0.75$, $\zeta = q^{\text{ampl}}/p^{\text{av}}$). Black solid curves = recalculation with HCA model and parameters in columns 14 to 20 of Table 2. Gray dashed curves = recalculation with parameters estimated from correlations (2) to (8).

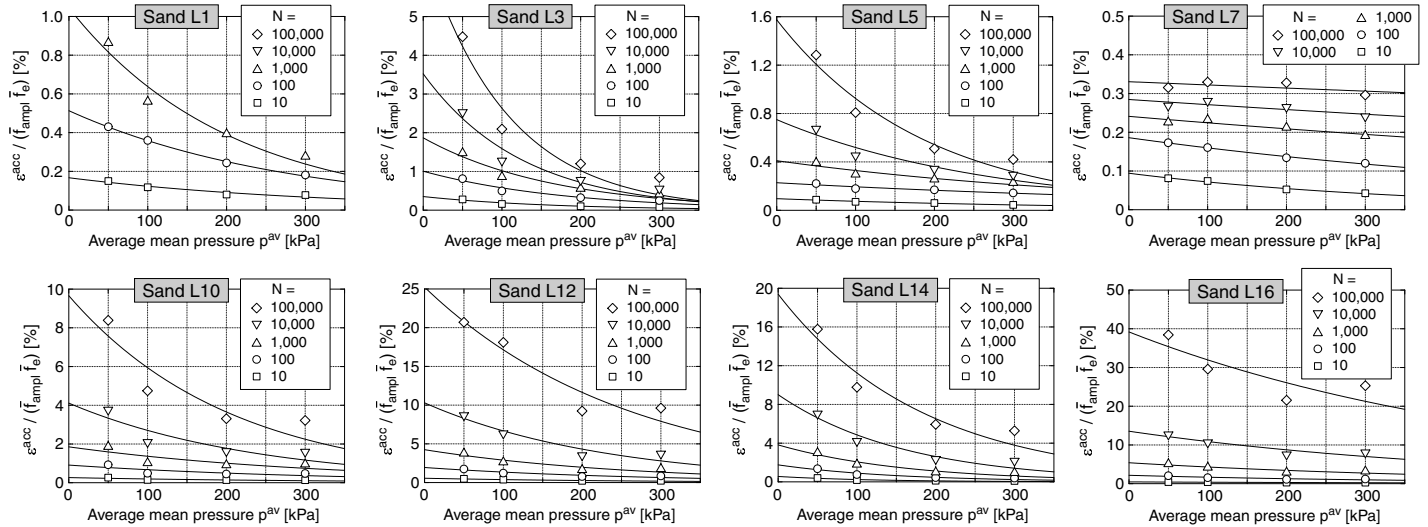


Fig. 13: Accumulated strain $\varepsilon^{\text{acc}}/(\bar{f}_{\text{ampl}}\bar{f}_e)$ as a function of average mean pressure p^{av} (solid curves = fitting of HCA model function f_p , see Table 1)

numbers of cycles as a function of the normalized average stress ratio \bar{Y}^{av} , respectively ($\bar{Y}^{\text{av}} = 0$ for isotropic stresses, $\bar{Y}^{\text{av}} = 1$ on the critical state line, see [24]).

The shape of the curves $\varepsilon^{\text{acc}}(N)$ can be judged from Figures 7, 10, 12 and 14, and from Figure 16 where the $\varepsilon^{\text{acc}}(N)$ data have been divided by the functions \bar{f}_{ampl} , \bar{f}_e , f_p and f_Y of the HCA model (calculated with the constants given in columns 7 to 13 of Table 2), that means the data were purified from the influences of amplitude, void ratio and average stress. For uniform sands ($C_u \leq 2$) the permanent strain increases almost proportional to $\ln(N)$ up to at least $N = 10^4$ cycles. At $N > 10^4$ for some of the sands L1 to L7 (see e.g. L1 and L3 in Figure 7) the permanent strain grows faster than proportional to $\ln(N)$. With increasing grain size of the uniform granular material the accumulation curves $\varepsilon^{\text{acc}}(N)$ up to $N = 10^5$ become more and more linear in the semi-logarithmic scale. For the coarsest

tested material L7 they are almost perfectly linear in most tests. The curves $\varepsilon^{\text{acc}}(N)$ for the more well-graded sands ($C_u \geq 2.5$) show a curvature in the log-linear plots, which becomes more pronounced with increasing uniformity coefficient C_u (compare e.g. the data for L10 and L16 in Figures 7, 10, 12 and 14). These findings show that the shape of the permanent strain accumulation curves $\varepsilon^{\text{acc}}(N)$ significantly depends on the grain size distribution curve of the tested material, which confirms the results of the earlier study documented by Wichtmann et al. [24].

Differences in the shape of the accumulation curves reported in the literature - sometimes logarithmic functions $\varepsilon^{\text{acc}} \sim \ln(N)$ and sometimes power laws $\varepsilon^{\text{acc}} \sim N^a$ are reported suitable to approximate the measured curves $\varepsilon^{\text{acc}}(N)$ - may thus be due to the different grain size distribution curves of the tested materials. Based on the present test data, logarithmic functions seem not to be suitable for

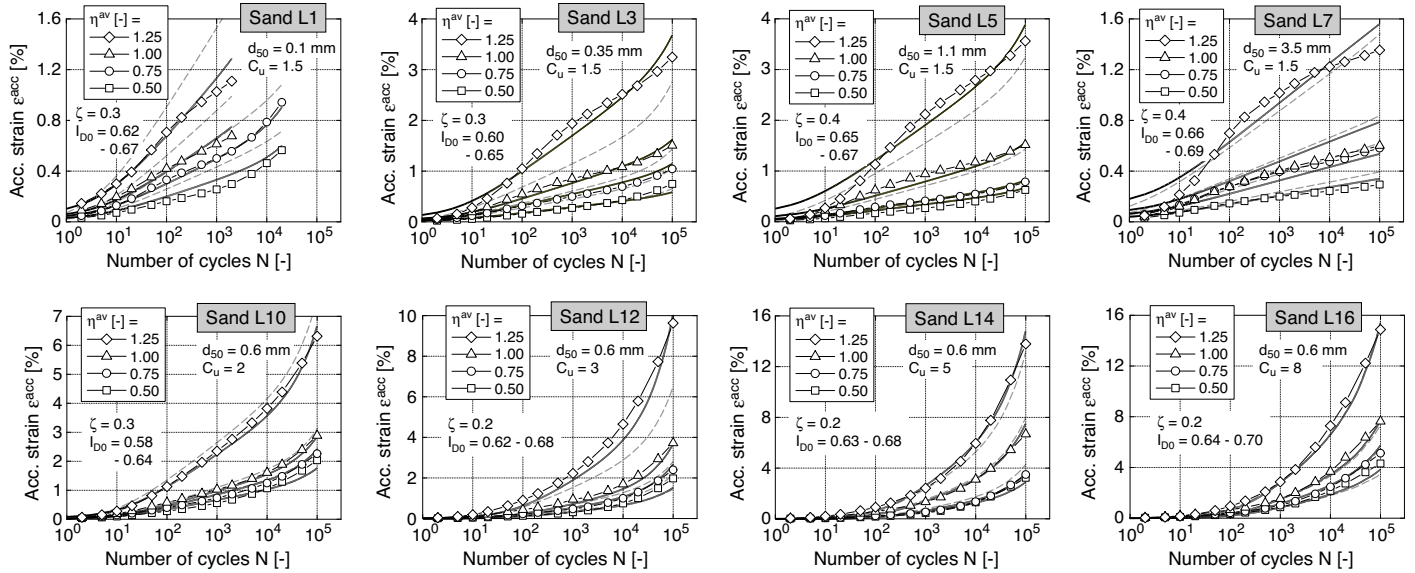


Fig. 14: Accumulation curves $\varepsilon^{acc}(N)$ measured in tests with different average stress ratios η^{av} (all tests: $p^{av} = 200$ kPa). Black solid curves = recalculation with HCA model and parameters in columns 14 to 20 of Table 2. Gray dashed curves = recalculation with parameters estimated from correlations (2) to (8).

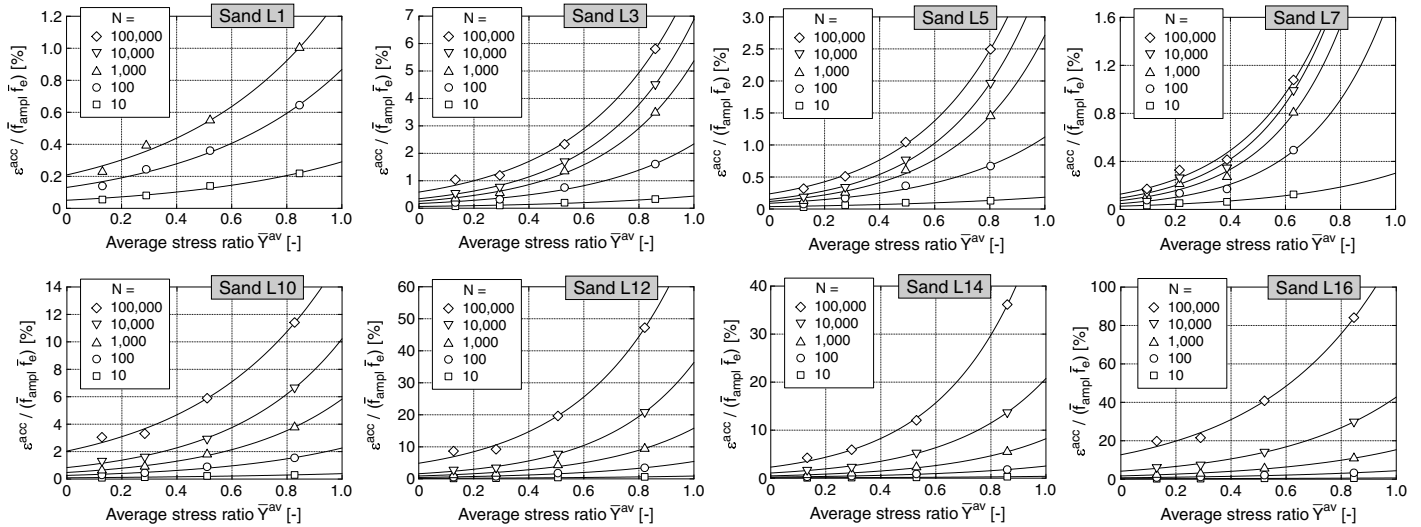


Fig. 15: Accumulated strain $\varepsilon^{acc}/(\bar{f}_{ampl}\bar{f}_e)$ as a function of normalized average stress ratio \bar{Y}^{av} (solid curves = fitting of HCA model function f_Y , see Table 1)

well-graded sands (e.g. L12 - L16 in Figure 7) while power laws are inappropriate for coarse uniform materials (e.g. L7 in Figure 7). In contrast, the function f_N used in the HCA model of Niemunis et al. [16], consisting of a logarithmic and a linear portion, is flexible enough to approximate various shapes of measured $\varepsilon^{acc}(N)$ curves satisfactorily (see recalculations of tests discussed in the next section).

4 Determination of HCA model parameters and recalculations of tests

In the HCA model of Niemunis et al. [16] the intensity of accumulation is described by the following equation

$$\dot{\varepsilon}^{acc} = f_{ampl} \dot{f}_N f_e f_p f_Y f_\pi \quad (1)$$

The factors of Eq. (1) are summarized in Table 1. The revision of the amplitude function f_{ampl} compared to [16] is commented below. The factor f_π for polarization changes

Function	Const.
$f_{ampl} = (\varepsilon^{ampl}/10^{-4})^{C_{ampl}}$	C_{ampl}
$\dot{f}_N = \frac{C_{N1}C_{N2}}{1 + C_{N2}N} + C_{N1}C_{N3}$	C_{N1}, C_{N2}, C_{N3}
$f_p = \exp[-C_p (p^{av}/(100 \text{ kPa}) - 1)]$	C_p
$f_Y = \exp(C_Y Y^{av})$	C_Y
$f_e = \frac{(C_e - e)^2}{1 + e} \frac{1 + e_{max}}{(C_e - e_{max})^2}$	C_e

Table 1: Summary of the functions and material constants of the HCA model

is equal to 1 for the triaxial tests with uniaxial (vertical) cyclic loading performed in this study. The function \dot{f}_N for the influence of cyclic preloading given in Table 1 applies

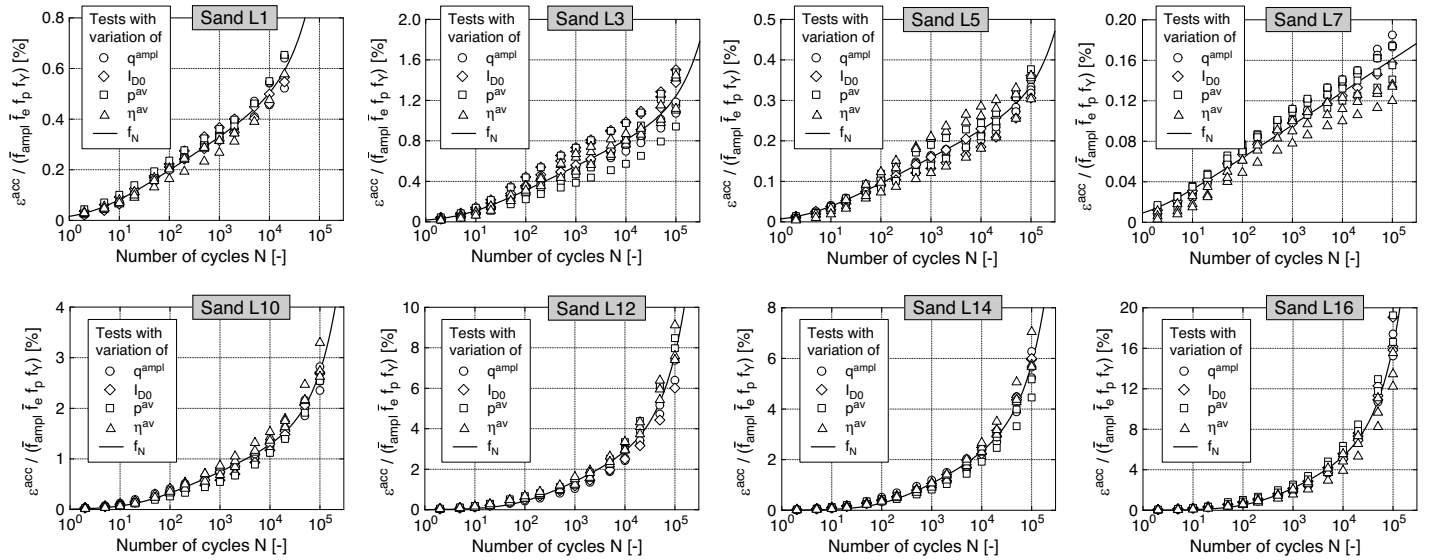


Fig. 16: Curves $\varepsilon^{acc}(N)/(\bar{f}_{ampl}\bar{f}_e\bar{f}_p\bar{f}_y)$, fitting of function $f_N = C_{N1} [\ln(1 + C_{N2}N) + C_{N3}N]$

for the simplest case of a cyclic loading with constant strain amplitude ε^{ampl} only. For the general formulation using a preloading variable g^A it is referred to [16]. Based on the data shown in Figures 8, 11, 13, 15 and 16, the parameters of the HCA model have been first determined "by hand" as described in [24, 25].

As mentioned above not all materials tested in the present study obeyed the relationship $\varepsilon^{acc} \sim (\varepsilon^{ampl})^2$, i.e. a square dependence of the strain accumulation rate on strain amplitude. Up to now such relationship with a fixed exponent 2 had been implemented into the HCA model [24, 25]. In order to enable the HCA model to reproduce the present test results, an additional material constant C_{ampl} has now been introduced according to $\varepsilon^{acc} \sim (\varepsilon^{ampl})^{C_{ampl}}$. In contrast to [24, 25], the amplitude function f_{ampl} of the HCA model is thus defined as $f_{ampl} = (\varepsilon^{ampl}/10^{-4})^{C_{ampl}}$ in the following (see Table 1). The additional material parameter in f_{ampl} renders the calibration procedure somewhat more laborious. Since f_{ampl} is necessary to purify the data in Figure 11 and f_e is used on the ordinate in Figure 8, the determination of the parameters C_{ampl} and C_e has now to be done by iteration. Having determined C_{ampl} and C_e , the remaining parameters C_p , C_Y , C_{N1} , C_{N2} and C_{N3} can be obtained as described in [25]. All parameters determined "by hand" for the 14 sands L1 - L7 and L10 - L16 tested in this study are given in columns 7 to 13 of Table 2. The test data for the eight sands S1 - S8 documented in [24] have also been re-analyzed allowing $C_{ampl} \neq 2.0$. The HCA model parameters obtained for these sands are also provided in Table 2. For the 22 sands in Table 2, the parameter C_{ampl} takes values between 1.43 and 2.22 which justifies the introduction of this parameter in the HCA model.

After having calibrated all parameters "by hand", a fine-tuning of the sets of parameters using an element test program with an automated optimization algorithm was undertaken. It should be noted that this element test program is not based on Niemunis' Incremental Driver [15]. While Incremental Driver can be used to check conventional constitutive models (in the context of HCA models used for the so-called "implicit" phases of the calculation), the element

test program applied in the present study is customized for simulations with the HCA model. The program implements the equations of the HCA model, i.e. it calculates only the development of residual strain with increasing number of cycles. The boundary and initial conditions of each test (p^{av} , η^{av} , e_0) and the measured strain amplitude $\varepsilon^{ampl}(N)$ are used as input, while the accumulation curves $\varepsilon^{acc}(N)$ are received as output.

The user specifies minimum and maximum values for each HCA model parameter, as well as an increment. These values can be chosen based on the parameters obtained from the previous by hand calibration. The algorithm calculates the accumulation curves $\varepsilon^{acc}(N)$ for all combinations of the HCA model parameters within the specified limits, using the prescribed increments. From all tested combinations the set of parameters with the smallest deviations between the predicted ε^{acc} values and the residual strains measured in the laboratory tests is chosen as the optimum one. This deviation is judged by summing up the squared errors calculated for all data points (N , ε^{acc}) involved in the simulation. The algorithm is robust, that means it always finds the global minimum of the sum of the squared errors within the specified limits of the parameters. However, it is not immune against an inappropriate choice of the limits or too large increments of the parameters. A minimization of the sum of *absolute* error values has been also tried out with the element test program. However, the parameters hardly differed from those obtained for squared errors.

It is convenient to optimize the parameters C_{ampl} , C_e , ... one after another. For example, in order to determine the optimum value of C_{ampl} , the simulations can be restricted to the tests with different stress amplitudes. The parameters C_{ampl} and C_{N1} (a second degree of freedom is necessary) are then varied within the specified limits while all other parameters C_e , C_p , ... are kept constant on their values previously determined in the by hand calibration. Afterwards the parameter C_e can be optimized, by simulating the tests with different densities and varying C_e and C_{N1} . An optimization of C_p and C_Y in a similar manner follows. Finally, the parameters C_{N1} , C_{N2} and C_{N3} are optimized by recalculating all element tests available for

a certain material. While C_{ampl} , C_e , C_p and C_Y are kept constant on their previously determined optimum values in these simulations, the parameters C_{N1} , C_{N2} and C_{N3} are varied until the best approximation of the experimental data is found. The parameters given in columns 14 - 20 of Table 2 have been determined in such a consecutive procedure.

The optimized parameters differ slightly from those obtained "by hand" due to some simplifications of the "by hand" method [25]. The span of C_{ampl} (1.33 to 2.43) is even larger in case of the parameters optimized by the element test program.

The accumulation curves $\varepsilon^{\text{acc}}(N)$ resulting from a recalculation of the laboratory tests with the HCA model using the parameters in columns 14 to 20 of Table 2 have been added as black solid curves in Figures 7, 10, 12 and 14. In most cases the differences between the experimental and the calculated data are small, confirming the good prediction of the HCA model. For some sands slightly too low accumulation rates are predicted for small pressures (Figure 12), due to deficits of the function f_p of the HCA model [24]. The parameters determined "by hand" (columns 7 to 13 of Table 2) deliver a similar prediction.

5 Simplified calibration procedure

In [24] correlations of the HCA model parameters with d_{50} , C_u and e_{min} have been developed since these three quantities can be easily determined by standard laboratory tests. Furthermore, the HCA model parameter C_e can be interpreted as the minimum void ratio that can be reached by cyclic loading, since the rate of accumulation vanishes in case $e = C_e$. Therefore, it is reasonable to correlate C_e with the minimum void ratio e_{min} obtained from standard procedures. For the linear grain size distribution curves tested in the present study the curvature index $C_c = (d_{30})^2/(d_{10}d_{60})$ is directly related to C_u according to $C_c = (1/C_u)^{1/5}$, lying in the range $0.66 \leq C_c \leq 0.92$ for all tested materials. Therefore, the influence of C_c on the HCA model parameters cannot be quantified independently. In order to keep the correlations as simple as possible they have been only formulated with d_{50} , C_u and e_{min} .

In Figure 17 the HCA model parameters C_{ampl} , C_e , C_p , C_Y , C_{N1} , C_{N2} and C_{N3} determined for the 22 sands (Table 2) are plotted versus mean grain size d_{50} , uniformity coefficient C_u or minimum void ratio e_{min} , respectively.

The parameter C_{ampl} correlates neither with d_{50} nor with C_u (Figure 17a,b). The diagram in Figure 17a contains only the data for the uniform sands or gravels L1 to L7 and S1 to S6, i.e. materials with C_u -values within a relatively narrow range ($1.4 \leq C_u \leq 1.9$). The diagram in Figure 17b collects the data for the sands L4, L10 to L16 and S3, S7 and S8 with similar values of mean grain size ($0.52 \text{ mm} \leq d_{50} \leq 0.60 \text{ mm}$). Therefore, in both diagrams one parameter of the grain size distribution curve has been kept approximately constant while the other one varies significantly ($0.1 \text{ mm} \leq d_{50} \leq 3.5 \text{ mm}$ in Figure 17a, $1.5 \leq C_u \leq 8$ in Figure 17b). However, no clear tendencies concerning a dependence of C_{ampl} on d_{50} or C_u can be observed in these two diagrams. Therefore, for a simplified calibration it is recommended to use the mean value of all tested materials (solid line in Figure 17a,b):

$$C_{\text{ampl}} = 1.70 \quad (2)$$

Obviously, this mean value is lower than the constant exponent $C_{\text{ampl}} = 2$ implemented in the HCA model so far. The parameter C_e decreases with increasing mean grain size and with increasing uniformity coefficient, at least up to $C_u = 5$ (Figure 17c,d). A correlation of C_e with e_{min} is provided in Figure 17e and can be described by

$$C_e = 0.95 \cdot e_{\text{min}} \quad (3)$$

(solid line in Figure 17e). The values of C_p and C_Y plotted in Figure 17f-i were determined from a new analysis of the test data with C_{ampl} and C_e calculated from Eqs. (2) and (3). Hardly any dependence of C_p and C_Y on the uniformity coefficient could be found (Figure 17g,i). C_p decreases with increasing mean grain size (Figure 17f) which can be approximated by

$$C_p = 0.41 \cdot [1 - 0.34 (d_{50}[\text{mm}] - 0.6)] \quad (4)$$

(solid curve in Figure 17f). According to Eq. (4), the intensity of accumulation is independent of the average mean pressure for a mean grain size $d_{50} \approx 3.5 \text{ mm}$. This agrees well with the data for the fine gravel L7 (Figure 13). The increase of ε^{acc} with increasing p^{av} predicted by Eq. (4) for $d_{50} > 3.5 \text{ mm}$ has not been confirmed experimentally yet. The larger parameters C_Y for larger mean grain sizes are captured by the following correlation (solid curve in Figure 17h):

$$C_Y = 2.60 \cdot [1 + 0.12 \ln(d_{50}[\text{mm}]/0.6)] \quad (5)$$

The data for C_{N1} , C_{N2} and C_{N3} in Figure 17j-o have been obtained from a re-analysis of the test data with C_{ampl} , C_e , C_p and C_Y calculated from Eqs. (2) to (5). C_{N1} decreases with increasing mean grain size and increases with increasing uniformity coefficient (Figure 17j,k). C_{N2} increases with d_{50} and decreases with C_u (Figure 17l,m) while C_{N3} decreases with d_{50} and increases with C_u (Figure 17n,o). The large scatter of data in Figure 17n is due to the fact, that for uniform sands C_{N3} describes the accumulation rates at large numbers of cycles and could be better evaluated from long-term tests with $N > 10^5$ cycles. The data in Figure 17j-o can be approximated by the following equations (solid curves):

$$C_{N1} = 4.5 \cdot 10^{-4} \cdot [1 - 0.306 \ln(d_{50}[\text{mm}]/0.6)] \cdot [1 + 3.15 (C_u - 1.5)] \quad (6)$$

$$C_{N2} = 0.31 \cdot \exp[0.39 (d_{50}[\text{mm}] - 0.6)] \cdot \exp[12.3(\exp(-0.77C_u) - 0.315)] \quad (7)$$

$$C_{N3} = 3.0 \cdot 10^{-5} \cdot \exp[-0.84 (d_{50}[\text{mm}] - 0.6)] \cdot [1 + 7.85 (C_u - 1.5)]^{0.34} \quad (8)$$

Since the experimental data for $C_u < 1.5$ is limited, it is recommended to evaluate Eqs. (6) to (8) with $C_u = 1.5$ in case of sands with $C_u < 1.5$. The curve-fitting leading to Eqs. (2) to (8), i.e. to the solid curves in Figure 17 has been performed using the program Origin with the method of least squares and the Levenberg-Marquardt algorithm for iterations. Alternatively, a curve-fitting with a minimization of the absolute errors has been also performed, resulting into the dashed curves in Figure 17. Although the absolute error method is less susceptible for outliers, the solid and the dashed curves in Figure 17 do not differ much in most cases. The largest differences are obtained for the parameter C_{N1} at low d_{50} values (about 7 %) and for C_{N2} at

1	2	3	4	5	6	7	8	9	10	11	12	13	14	15	16	17	18	19	20
Sand	d_{50}	C_u	e_{min}	$e_{max} = e_{ref}$	φ_c	calibrated "by hand"			according to procedure in [25]			optimized with element test program							
	[mm]	[-]	[-]	[-]	[°]	C_{ampl}	C_e	C_p	C_Y	C_{N1}	C_{N2}	C_{N3}	C_{ampl}	C_e	C_p	C_Y	C_{N1}	C_{N2}	C_{N3}
						[-]	[-]	[-]	[-]	[10 ⁻⁴]	[-]	[10 ⁻⁵]	[-]	[-]	[-]	[-]	[10 ⁻⁴]	[-]	[10 ⁻⁵]
L1	0.1	1.5	0.634	1.127	33.4	1.60	0.60	0.40	1.84	5.61	0.328	8.79	1.69	0.60	0.40	1.99	0.485	0.30	10.5
L2	0.2	1.5	0.596	0.994	32.9	1.43	0.64	0.29	1.94	16.8	0.137	5.37	1.33	0.65	0.30	1.89	18.0	0.15	6.0
L3	0.35	1.5	0.591	0.931	33.1	1.76	0.59	0.69	2.72	10.5	0.185	2.02	1.85	0.61	0.55	3.00	8.25	0.24	2.1
L4	0.6	1.5	0.571	0.891	32.8	1.92	0.55	0.53	2.52	5.07	0.197	2.76	1.97	0.57	0.52	2.82	4.35	0.30	3.5
L5	1.1	1.5	0.580	0.879	33.6	1.77	0.52	0.29	2.77	2.77	0.303	1.86	1.84	0.54	0.32	3.14	2.50	0.54	2.0
L6	2.0	1.5	0.591	0.877	35.0	1.70	0.56	0.12	2.57	3.01	0.576	0	1.64	0.58	0.11	2.72	3.66	0.89	0.1
L7	3.5	1.5	0.626	0.817	36.4	1.46	0.51	0.11	3.49	1.41	0.907	0	1.48	0.51	0.09	3.49	1.28	0.96	0
L10	0.6	2	0.541	0.864	33.1	1.53	0.53	0.36	2.21	19.3	0.0439	5.74	1.67	0.53	0.32	2.37	13.4	0.075	5.5
L11	0.6	2.5	0.495	0.856	33.2	2.03	0.50	0.42	2.41	23.3	0.0257	8.18	2.43	0.53	0.50	2.89	15.4	0.040	13.5
L12	0.6	3	0.474	0.829	33.6	1.40	0.47	0.39	2.70	51.4	0.0131	7.74	1.60	0.48	0.44	3.02	36.0	0.016	10.5
L13	0.6	4	0.414	0.791	33.6	1.68	0.40	0.39	2.44	53.6	0.00969	6.85	1.85	0.40	0.34	3.12	26.6	0.0090	10.0
L14	0.6	5	0.394	0.749	33.1	2.06	0.32	0.66	2.67	46.6	0.00817	5.70	2.34	0.34	0.45	3.29	23.0	0.0065	7.5
L15	0.6	6	0.387	0.719	33.0	1.76	0.33	0.55	2.15	68.6	0.00732	6.67	1.97	0.34	0.44	2.69	41.2	0.0070	7.5
L16	0.6	8	0.356	0.673	33.2	1.36	0.31	0.23	1.99	107	0.00611	8.78	1.53	0.31	0.23	2.45	79.2	0.0050	8.0
S1	0.15	1.4	0.612	0.992	32.0	1.48	0.59	0.27	1.76	8.58	0.266	3.27	1.50	0.57	0.33	1.69	8.20	0.28	2.5
S2	0.35	1.9	0.544	0.930	32.7	1.50	0.56	0.55	2.56	9.04	0.264	1.17	1.56	0.50	0.51	2.92	5.10	0.32	0.5
S3	0.55	1.8	0.577	0.874	31.2	1.70	0.54	0.28	1.85	4.42	0.402	4.77	1.76	0.53	0.42	2.06	3.60	0.42	5.0
S4	0.84	1.4	0.572	0.878	32.9	2.22	0.56	0.67	2.82	2.24	0.426	3.30	2.13	0.58	0.49	3.19	2.90	0.38	2.5
S5	1.45	1.4	0.574	0.886	33.2	1.64	0.48	0.33	2.52	3.30	0.534	0	1.74	0.53	0.35	2.78	3.40	0.84	0
S6	4.4	1.3	0.622	0.851	37.2	1.47	0.42	0.09	2.85	0.79	1.187	0	1.38	0.41	-0.04	2.84	0.72	1.24	0
S7	0.55	3.2	0.453	0.811	33.1	1.56	0.44	0.48	2.00	54.4	0.024	5.60	1.83	0.45	0.52	2.76	2.90	0.04	8.0
S8	0.52	4.5	0.383	0.691	34.2	1.72	0.36	0.48	2.82	94.7	0.0055	6.91	1.89	0.36	0.50	3.76	52.0	0.0045	4.5

Table 2: HCA model parameters for the 14 sands L1 - L7 and L10 - L16 tested in the present study and for the eight sands S1 - S8 from [24] (data re-analyzed with $C_{ampl} \neq 2.0$). The minimum and maximum void ratios e_{min} and e_{max} were determined according to German standard code DIN 18126. φ_c is the critical friction angle.

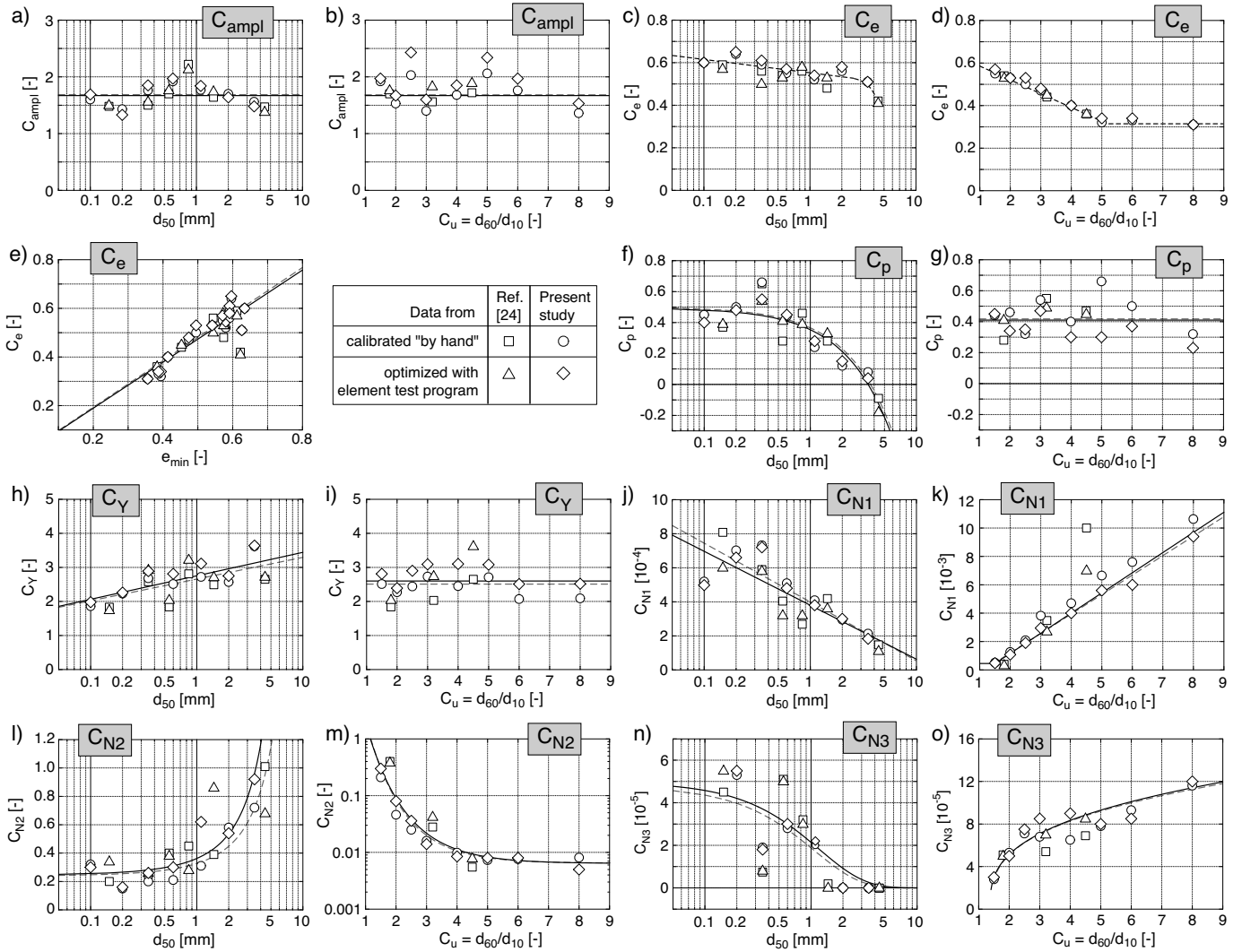


Fig. 17: Correlations of the HCA model parameters C_{ampl} , C_e , C_p , C_Y , C_{N1} , C_{N2} and C_{N3} with d_{50} , C_u or e_{min} , respectively. Black solid curves = Eqs. (2) to (8), determined from a curve-fitting minimizing squared errors. Gray dashed curves = results of curve-fitting minimizing the absolute values of errors.

large mean grain sizes (about 35 %, relating to the values from the least squares fitting). However, since it is recommended to determine the parameters C_{N1} and C_{N2} from laboratory tests (see remarks below) and to use Eqs. (6) and (7) for rough estimations in preliminary studies only, these differences are of minor importance.

For a given sand, the HCA model parameters C_{amp1} , C_e , C_p , C_Y , C_{N1} , C_{N2} and C_{N3} can be determined in different ways, with different experimental effort and accuracy:

1. All parameters are determined in drained cyclic triaxial tests.
2. Some parameters are estimated from Eqs. (2) to (8) while the other ones are determined in drained cyclic triaxial tests. Figure 18 shows the variation of the accumulation curves predicted by the HCA model if a single parameter is either increased or decreased by 10 % (sensitivity analysis). Obviously the model prediction is very sensitive to changes in C_e . Therefore, two important cases of a mixed determination procedure are:

- The parameters C_{amp1} , C_e , C_p and C_Y are estimated from Eqs. (2) to (5). The parameters C_{N1} , C_{N2} and C_{N3} are determined from a single cyclic test.
- The parameters C_{amp1} , C_p and C_Y are estimated from Eqs. (2), (4) and (5). The parameters C_e , C_{N1} , C_{N2} and C_{N3} are determined from at least three tests with different initial densities.

These two procedures are recommended if the number of cyclic laboratory tests has to be kept at a minimum.

3. All parameters are estimated from the correlations given by Eqs. (2) to (8). This option is recommended only for very rough estimations, e.g. in the preliminary design phase of foundations subjected to high-cyclic loading.

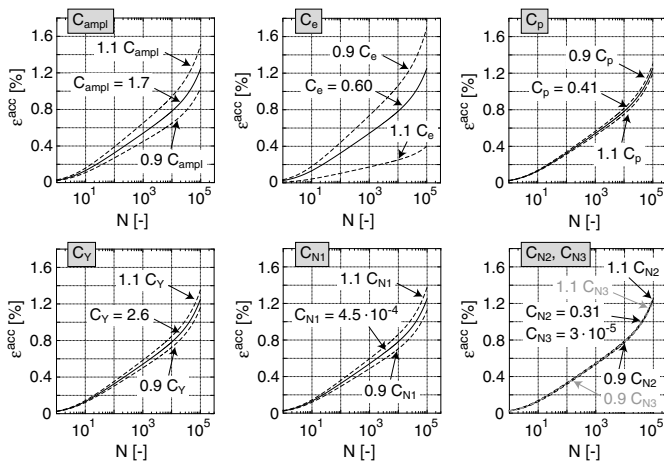


Fig. 18: The solid curve $\varepsilon^{acc}(N)$ (same in all diagrams) is predicted by the HCA model for $p^{av} = 200$ kPa, $\eta^{av} = 0.75$, $e_0 = 0.70$ and $\varepsilon^{amp1} = 3 \cdot 10^{-4}$ using parameters calculated from Eqs. (2) - (8) for a sand having $d_{50} = 0.6$ mm and $C_u = 1.5$. The dashed or dot-dashed curves were generated with a single parameter decreased or increased by 10 %.

6 Comparison of old [24] and new correlations by means of statistical measures

In Table 3 the new correlations (2) to (8) are compared to those proposed in [24] by means of different statistical parameters defined as follows (x_i = independent variable, y_i = dependent variable, $f(x_i)$ = model prediction, $i = 1, 2, \dots, N$):

- Standard deviation of the residuals (chi-square divided by the number of degrees of freedom, $DOF = \text{number of data points} - \text{number of fitting parameters}$):

$$\frac{\chi^2}{DOF} \quad \text{with} \quad \chi^2 = \sum_i^N [y_i - f(x_i)]^2 \quad (9)$$

- Goodness of fit (\bar{y} = mean value of all y_i values):

$$R^2 = 1 - \frac{\chi^2}{\sum [y_i - \bar{y}]^2} \quad (10)$$

- Mean deviation:

$$MD = \frac{1}{N} \sum_{i=1}^N |f(x_i) - y_i| \quad (11)$$

- Root mean squared error:

$$RMSE = \sqrt{\chi^2/N} \quad (12)$$

The lower the values of χ^2/DOF , MD or $RMSE$ and the higher the R^2 value are, the better is the fitting of the data by the chosen function.

Note that R^2 is approximately zero if the data for a certain parameter do not show any clear tendencies with d_{50} and C_u and thus has been approximated by constant values. In that case $f(x_i)$ and \bar{y} are almost identical, leading to $R^2 \approx 0$ according to Eq. (10). For example, in [24] constant values have been proposed for an estimation of C_p and C_Y . Consequently, the corresponding R^2 values in Table 3 are almost zero. The relatively low value of $R^2 = 0.31$ in case of C_Y determined from Eq. (5) is due to similar reasons: The d_{50} -dependence is relatively small (Figure 17h) and no C_u -influence can be found in the data (Figure 17i). If only the $C_Y(d_{50})$ data in Figure 17h are analyzed, letting away the $C_Y(C_u)$ values in Figure 17i, a somewhat larger $R^2 = 0.46$ is obtained. In such cases of almost constant or only slightly varying data the quality of a curve-fitting can be better judged by other parameters like χ^2/DOF , MD or $RMSE$.

Regression error characteristic (REC) curves have been plotted in Figure 19. These curves show the percentage of data predicted within a certain tolerance versus the tolerance $|f(x_i) - y_i|$. The diagrams compare the REC curves obtained from Eqs. (3) - (8) and the data in Figure 17 with those generated based on the correlations and data presented in [24]. Looking at Table 3 and Figure 19, the new correlations (2) - (8) seem to have no clear advantage over those proposed in [24]. However, apart from the fact that Eqs. (2) - (8) are based on significantly more experimental data, as discussed in the next section the new correlations deliver a much better prediction for well-graded granular materials.

		C_e	C_p	C_Y	C_{N1}	C_{N2}	C_{N3}
χ^2	(2)-(8)	0.0014	0.010	0.157	$9.4 \cdot 10^{-7}$	0.013	$3.0 \cdot 10^{-10}$
χ^2	[24]	0.0002	0.027	0.237	$7.3 \cdot 10^{-7}$	0.013	$3.5 \cdot 10^{-10}$
R^2	(2)-(8)	0.86	0.71	0.31	0.90	0.79	0.76
R^2	[24]	0.96	0.00	-0.01	0.94	0.94	0.63
MD	(2)-(8)	0.0268	0.079	0.321	$4.4 \cdot 10^{-4}$	0.068	$1.1 \cdot 10^{-5}$
MD	[24]	0.0117	0.115	0.400	$3.9 \cdot 10^{-7}$	0.068	$1.1 \cdot 10^{-5}$
$RMSE$	(2)-(8)	0.0356	0.096	0.388	$9.4 \cdot 10^{-4}$	0.109	$1.6 \cdot 10^{-5}$
$RMSE$	[24]	0.0141	0.154	0.456	$6.8 \cdot 10^{-4}$	0.092	$1.5 \cdot 10^{-5}$

Table 3: Statistical parameters evaluated for the correlations (2) - (8) and for the correlations proposed in [24]

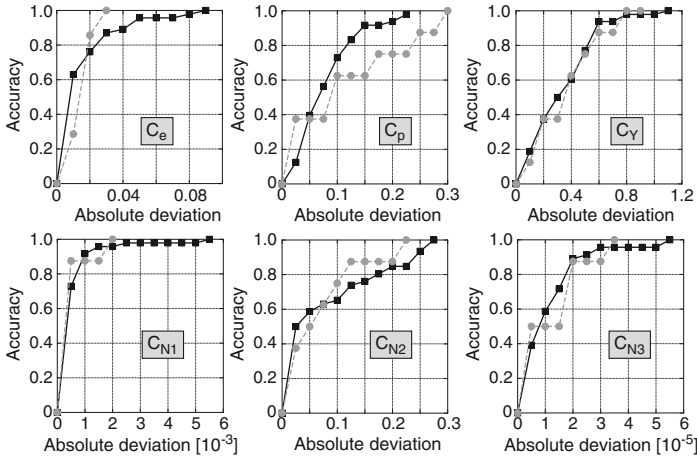


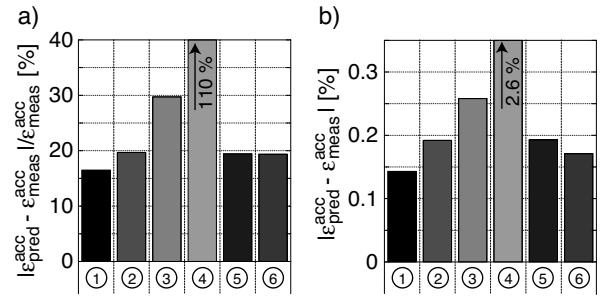
Fig. 19: REC curves showing the percentage of data predicted within a certain tolerance (accuracy) versus the tolerance $|f(x_i) - y_i|$ (absolute deviation). Black solid curves: Correlations (2)-(8); Gray dashed curves: Correlations from [24].

7 Inspection of prediction quality using (partly) estimated HCA model parameters

The prediction quality of the HCA model with parameters determined in different ways has been inspected by recalculations of the laboratory tests. The bar charts in Figure 20 show the average values of the deviation between predicted (ε_{pred}^{acc}) and measured (ε_{meas}^{acc}) permanent strain, either in percentage ($|\varepsilon_{pred}^{acc} - \varepsilon_{meas}^{acc}| / \varepsilon_{meas}^{acc}$, Figure 20a) or in absolute values ($|\varepsilon_{pred}^{acc} - \varepsilon_{meas}^{acc}|$, Figure 20b). Figure 20 is based on the data of all 22 sands at cycle numbers $N = 10^2, 10^3, 10^4$ and 10^5 . Obviously, the best prediction is achieved if all parameters are determined from cyclic tests. The parameters optimized with the element test program (first column in Figure 20, parameters from columns 14 - 20 in Table 2) deliver a slightly better prediction than the parameters calibrated "by hand" (second column in Figure 20, parameters from columns 7 - 13 in Table 2). In both cases the deviations are due to the scatter of experimental data or deficits of the HCA model functions (i.e. f_p at $p = 50$ kPa) only.

The prediction is less accurate if all parameters are determined from the correlations (2) - (8) (third column in Figure 20). The accumulation curves $\varepsilon^{acc}(N)$ predicted by the HCA model with all parameters estimated from the correlations (2) to (8) have been also added as gray dashed curves in Figures 7, 10, 12 and 14. The lower prediction quality is also obvious in those figures.

The permanent strains measured for the more well-graded granular materials L14, L15 and L16 ($C_u \geq 5$) are significantly over-estimated by the correlations proposed



Parameters determined from

- ① cyclic tests, optimized with element test program (Table 2, columns 14-20)
- ② cyclic tests, calibrated by hand (Table 2, columns 7-13)
- ③ correlations (2) - (8)
- ④ correlations proposed in [24]
- ⑤ C_{ampl}, C_e, C_p, C_Y from correlations (2) - (5), C_{N1}, C_{N2}, C_{N3} from a single cyclic test (optimized)
- ⑥ C_{ampl}, C_p, C_Y from correlations (2), (4) and (5), $C_e, C_{N1}, C_{N2}, C_{N3}$ from the test series with different I_{D0} (optimized)

Fig. 20: Average deviation between permanent strain ε_{pred}^{acc} predicted by the HCA model and measured permanent strain ε_{meas}^{acc} . The data from the 22 sands have been evaluated at $N = 10^2, 10^3, 10^4$ and 10^5 : a) Percentage values $|\varepsilon_{pred}^{acc} - \varepsilon_{meas}^{acc}| / \varepsilon_{meas}^{acc}$, b) Absolute values $|\varepsilon_{pred}^{acc} - \varepsilon_{meas}^{acc}|$

in [24] (average deviations in percentage: 114, 401 and 1902 % for L14, L15 and L16), leading to the large values of deviation in Figure 20 (fourth column). This is due to the fact that only tests on materials with $C_u < 5$ were available for the development of the correlations given in [24]. Therefore, it is strongly recommended to use the correlations (2) - (8) given in this paper instead of those proposed in [24], in particular for materials with $C_u \geq 5$.

The last two columns in Figure 20 belong to sets of parameters partially determined from cyclic tests and partially estimated from Eqs. (2) - (5). Either the parameters C_{N1}, C_{N2} and C_{N3} were determined from a single test on a medium dense sample with $p^{av} = 200$ kPa, $\eta^{av} = 0.75$ and $q^{ampl} = 40$ or 60 kPa (fifth column in Figure 20) or the parameters C_e, C_{N1}, C_{N2} and C_{N3} were obtained from the test series with a variation of initial relative density (last column in Figure 20). Although the experimental effort for the parameter calibration is much less in these two cases, the prediction is only slightly less accurate than in the case that all parameters are determined experimentally and optimized using the element test program. Therefore, a mixed calibration based on either a single test or three tests with different initial densities can be recommended for practical application.

The moderate loss of accuracy connected with the calibration based on a limited number of cyclic tests is acceptable considering the overall accuracy of geotechnical predictions. Furthermore, the appropriate determination of the initial relative density profile with depth may be of larger importance regarding a reliable settlement prediction with the HCA model compared to the uncertainties stemming from the parameter calibration procedure. In a future publication the different sources of uncertainty in connection with a prediction made with the HCA model will be discussed in the context of offshore wind power plant founda-

tions.

8 Summary, conclusions and outlook

The results of approx. 150 drained cyclic triaxial tests with 10^5 cycles performed on 14 clean quartz sands with different linear grain size distribution curves are presented. The tested materials had mean grain sizes in the range $0.1 \text{ mm} \leq d_{50} \leq 3.5 \text{ mm}$ and uniformity coefficients in the range $1.5 \leq C_u = d_{60}/d_{10} \leq 8$. For each material, tests with different stress amplitudes, initial densities and average stresses were performed.

The test results confirm the findings in [24] that the average stress ratio $\eta^{\text{av}} = q^{\text{av}}/p^{\text{av}}$ is the main influencing parameter regarding the *direction* of strain accumulation $\dot{\varepsilon}_q^{\text{acc}}/\dot{\varepsilon}_v^{\text{acc}}$. Variations of amplitude, density and average mean pressure p^{av} do not significantly affect $\dot{\varepsilon}_q^{\text{acc}}/\dot{\varepsilon}_v^{\text{acc}}$ (see also [26]). Similar to [24], an increase of the *intensity* of strain accumulation $\dot{\varepsilon}^{\text{acc}} = \partial \varepsilon^{\text{acc}}/\partial N$ with increasing strain amplitude, increasing void ratio, decreasing average mean pressure and increasing average stress ratio was found for all tested materials. Comparing the results for the various tested granular materials, an increase of the intensity of strain accumulation with decreasing mean grain size d_{50} and increasing uniformity coefficient C_u was observed. Furthermore, the curvature of the accumulation curves $\varepsilon^{\text{acc}}(N)$ in a log-linear plot was found to increase with increasing C_u .

Not all materials tested in the present study obeyed the relationship $\dot{\varepsilon}^{\text{acc}} \sim (\varepsilon^{\text{ampl}})^2$, i.e. a square dependence of the strain accumulation rate on strain amplitude. Up to now such relationship with a fixed exponent 2 had been implemented into the HCA model proposed by Niemunis et al. [25]. Consequently, an additional material constant C_{ampl} has been introduced into the HCA model describing the amplitude dependence according to $\dot{\varepsilon}^{\text{acc}} \sim (\varepsilon^{\text{ampl}})^{C_{\text{ampl}}}$. The parameters C_{ampl} , C_e , C_p , C_Y , C_{N1} , C_{N2} and C_{N3} of the HCA model have been calibrated based on the cyclic test data. The test data for eight sands documented in [24] have also been re-analyzed allowing $C_{\text{ampl}} \neq 2.0$. For the 22 sands, the parameter C_{ampl} takes values between 1.3 and 2.4 which justifies the introduction of this parameter in the HCA model.

For a simplified calibration, Wichtmann et al. [24] had proposed correlations of the HCA model parameters with d_{50} , C_u and e_{min} , based on the cyclic tests performed on eight sands. Due to the new parameter C_{ampl} these correlations had to be revised. Furthermore, they were extended by the data from the present study. It is demonstrated that the improved correlations (Eqs. (2) - (8)) deliver a more accurate prediction of the measured data than those proposed in [24], in particular for more well-graded granular materials ($C_u \geq 5$). Therefore, the use of the new correlations is recommended for a practical application. Furthermore, it has been demonstrated that the experimental effort can be significantly reduced without losing much prediction accuracy, if some HCA model parameters (C_e , C_{N1} , C_{N2} and C_{N3}) are determined from a limited number (one or three) of cyclic tests, while the other parameters are estimated from the correlations (2) - (8).

Finally, it should be stressed that the correlations (2) - (8) should only be applied within the range of tested d_{50} - and C_u -values, i.e. $0.1 \text{ mm} \leq d_{50} \leq 3.5 \text{ mm}$ and $C_u \leq 8$. Furthermore, at present these correlations are only valid

for clean quartz sands with subangular grain shape.

It is intended to extend the correlations presented in this paper in order to consider the influences of a fines content (up to now only clean quartz sands have been tested) and of the grain characteristics (e.g. shape, surface roughness, mineralogy). The respective experimental study will be presented in a separate publication in future.

9 Acknowledgments

The cyclic tests have been performed in the framework of the project A8 "Influence of the fabric changes in soil on the lifetime of structures" of special research field (SFB) 398 "Lifetime oriented design concepts" during the former work of the authors at Ruhr-University Bochum, Germany. Parts of the data analysis were undertaken in the framework of the project "Improvement of an accumulation model for high-cyclic loading" (TR 218/18-1). The authors are grateful to DFG (German Research Council) for the financial support of both projects. The cyclic triaxial tests have been performed by the laboratory technician M. Skubisch.

References

- [1] M. Abdelkrim, P. De Buhan, and G. Bonnet. A general method for calculating the traffic load-induced residual settlement of a platform, based on a structural analysis approach. *Soils and Foundations*, 46(4):401–414, 2006.
- [2] C.S. Chang and R.V. Whitman. Drained permanent deformation of sand due to cyclic loading. *Journal of Geotechnical Engineering, ASCE*, 114(10):1164–1180, 1988.
- [3] M.R. Cox and M. Budhu. A practical approach to grain shape quantification. *Engineering Geology*, 96:1–16, 2008.
- [4] S. Donohue, C. O'Sullivan, and M. Long. Particle breakage during cyclic triaxial loading of a carbonate sand. *Géotechnique*, 59(5):477–482, 2009.
- [5] P.M. Duku, J.P. Stewart, D.H. Whang, and E. Yee. Volumetric strains of clean sands subject to cyclic loads. *Journal of Geotechnical and Geoenvironmental Engineering, ASCE*, 134(8):1073–1085, 2008.
- [6] R. Galindo, M. Illueca, and R. Jimenez. Permanent deformation estimates of dynamic equipment foundations: Application to a gas turbine in granular soils. *Soil Dynamics and Earthquake Engineering*, 63(1):8–18, 2014.
- [7] S.J. Hain. An application of cyclic triaxial testing to field model test. In *International Symposium on Soils under cyclic and transient loading*, pages 23–31. Balkema, Rotterdam, Januar 1980. Swansea.
- [8] W.S. Kaggwa and J.R. Booker. Analysis of cyclic behaviour of calcareous sand. Technical Report 612, School of Civil and Mining Engineering, University of Sydney, Sydney, Australia, 1990.
- [9] W.S. Kaggwa, J.R. Booker, and J.P. Carter. Residual strains in calcareous sand due to irregular cyclic loading. *Journal of Geotechnical Engineering, ASCE*, 117(2):201–218, 1991.
- [10] C. Karg, S. Francois, W. Haegeman, and G. Degrande. Elasto-plastic long-term behavior of granular soils: modeling and experimental validation. *Soil Dynamics and Earthquake Engineering*, 30(8):635–646, 2010.
- [11] R. Katzenbach and G. Festag. Material behaviour of dry sand under cyclic loading. In T. Triantafyllidis, editor, *Cyclic behaviour of soils and liquefaction phenomena, Proc. of CBS04*, pages 153–158. Balkema, 2004.

- [12] S. López-Querol and M.R. Coop. Drained cyclic behaviour of loose Dogs Bay sand. *Géotechnique*, 62(4):281–289, 2012.
- [13] M.P. Luong. Mechanical aspects and thermal effects of cohesionless soils under cyclic and transient loading. In *Proc. IUTAM Conf. on Deformation and Failure of Granular materials, Delft*, pages 239–246, 1982.
- [14] W.A. Marr and J.T. Christian. Permanent displacements due to cyclic wave loading. *Journal of the Geotechnical Engineering Division, ASCE*, 107(GT8):1129–1149, 1981.
- [15] A. Niemunis. Incremental Driver User’s manual. , 2008. available from www.pg.gda.pl/~aniem/an-liter.html.
- [16] A. Niemunis, T. Wichtmann, and T. Triantafyllidis. A high-cycle accumulation model for sand. *Computers and Geotechnics*, 32(4):245–263, 2005.
- [17] C. Pasten, H. Shin, and J.C. Santamarina. Long-Term Foundation Response to Repetitive Loading. *Journal of Geotechnical and Geoenvironmental Engineering, ASCE*, 140(4), 2014.
- [18] A. Sawicki and W. Świdziński. Compaction curve as one of basic characteristics of granular soils. In E. Flavigny and D. Cordary, editors, *4th Colloque Franco-Polonais de Mécanique des Sols Appliquée*, volume 1, pages 103–115, 1987. Grenoble.
- [19] A. Sawicki and W. Świdziński. Mechanics of a sandy subsoil subjected to cyclic loadings. *Int. J. Numer. Anal. Meth. Geomech.*, 13:511–529, 1989.
- [20] M.L. Silver and H.B. Seed. Deformation characteristics of sands under cyclic loading. *Journal of the Soil Mechanics and Foundations Division, ASCE*, 97(SM8):1081–1098, 1971.
- [21] M.L. Silver and H.B. Seed. Volume changes in sands during cyclic loading. *Journal of the Soil Mechanics and Foundations Division, ASCE*, 97(SM9):1171–1182, 1971.
- [22] A.S.J. Suiker and R. de Borst. A numerical model for the cyclic deterioration of railway tracks. *International Journal for Numerical Methods in Engineering*, 57:441–470, 2003.
- [23] T. Wichtmann. Explicit accumulation model for non-cohesive soils under cyclic loading. PhD thesis, Publications of the Institute of Soil Mechanics and Foundation Engineering, Ruhr-University Bochum, Issue No. 38, 2005.
- [24] T. Wichtmann, A. Niemunis, and T. Triantafyllidis. Validation and calibration of a high-cycle accumulation model based on cyclic triaxial tests on eight sands. *Soils and Foundations*, 49(5):711–728, 2009.
- [25] T. Wichtmann, A. Niemunis, and T. Triantafyllidis. On the determination of a set of material constants for a high-cycle accumulation model for non-cohesive soils. *Int. J. Numer. Anal. Meth. Geomech.*, 34(4):409–440, 2010.
- [26] T. Wichtmann, A. Niemunis, and T. Triantafyllidis. Flow rule in a high-cycle accumulation model backed by cyclic test data of 22 sands. *Acta Geotechnica*, 9(4):695–709, 2014.
- [27] T. Wichtmann, A. Niemunis, and Th. Triantafyllidis. Towards the FE prediction of permanent deformations of offshore wind power plant foundations using a high-cycle accumulation model. In *International Symposium: Frontiers in Offshore Geotechnics, Perth, Australia*, pages 635–640, 2010.
- [28] T.L. Youd. Compaction of sands by repeated shear straining. *Journal of the Soil Mechanics and Foundations Division, ASCE*, 98(SM7):709–725, 1972.
- [29] H. Zachert, T. Wichtmann, T. Triantafyllidis, and U. Hartwig. Simulation of a full-scale test on a Gravity Base Foundation for Offshore Wind Turbines using a High Cycle Accumulation Model. In *3rd International Symposium on Frontiers in Offshore Geotechnics (ISFOG), Oslo*, 2015.